Bi-orthogonal Decomposition for Slow Acoustic Pulse Receptivity Simulation of Hypersonic Boundary Layer Over a Blunt Cone

Zihao Zou[*] and Simon He[†] Xiaolin Zhong[‡]
University of California, Los Angeles, California, 90095, USA

Boundary layer transition can be initiated differently given the nature of the external disturbances. Receptivity, which refers to the interaction between external disturbances and the boundary layer, introduces an initial disturbance amplitude into the flow for all scenarios. Different transition prediction tools consider receptivity to different extents. The popular e^N method primarily focuses on the growth rate, also called the N factor, of disturbances and neglects the initial amplitude. To address this issue, Mack (1977) proposed the amplitude method to incorporate receptivity, nonlinear effects, and broadband characteristics of disturbances. In amplitude method, an accurate evaluation of the receptivity coefficient at the branch I neutral stability location is significant in obtaining the initial amplitude of the disturbance wave. Current evaluation of the receptivity coefficient are the experimental fitting method used by Marineau (2017) and the back-tracking numerical method implemented by He and Zhong (2021). Although both approaches have the capability of obtaining the receptivity coefficient, the evaluation is not directly at the branch I neutral stability location for their case studies. Furthermore, the DNS results by He indicated a need for a multimode analysis to obtain the true initial amplitude at the branch I neutral stability location. To facilitate this analysis, the bi-orthogonal eigenfunction decomposition, proposed by Tumin (2007), can be applied to decompose the DNS flow field into normal modes including discrete and continuous modes to obtain the modal amplitude for receptivity evaluation. By employing the high order finite difference method by Zou and Zhong (2023), the bi-orthogonal eigenfunction system of the hypersonic boundary layer over a blunt cone is obtained, allowing for the decomposition of the receptivity flowfield. From the preliminary results of the decomposition, an overall trend of the discrete mode S amplitude and growth rate agrees with previous e^N and LST results, showing a reduction in multimode effects. The receptivity coefficient for a band of frequencies are also computed for demonstration. Moreover, in addition to the discrete modes F and S, a discrete entropy layer mode has been identified near the synchronization region. Decomposition results confirm that the discrete mode S being the dominant mode in downstream of the second mode unstable region while the discrete entropy layer mode and the discrete mode F both contribute to the flow near the synchronization region.

I. Introduction

Boundary layer transition has always been a critical topic of study in the field of fluid mechanics especially for the hypersonic flow over aerospace vehicles. Since the turbulent boundary layer can cause a higher aerodynamic drag and heating on a hypersonic vehicle, an accurate prediction on the laminar-turbulent transition location is crucial for the design of the vehicle in the placement of thermal protection. The study of stability of the boundary layer is divided into various paths depending on the amplitude of disturbance, depicted by Morkovin [1]. For all paths, the transition is initiated by the initial perturbations generated from ambient forcing disturbances through the receptivity mechanism. Depending on the amplitude of the disturbance, the instability waves can experience a linear modal growth, a transient growth of non-orthogonal modal interaction effect, or bypass to turbulence. In order to control and suppress the transition to turbulence, understanding the transition mechanism and its underlying pathways is paramount for controlling and suppressing turbulence onset.

This work focuses primarily on the small perturbation regime, which is closely resemble flight environments. In this regime, the disturbances from the freestream enter the boundary layer and give rise to initial perturbations during the

---

*Ph.D. Student, Mechanical and Aerospace Engineering, zzou1@ucla.edu, AIAA Student Member.
†Ph.D., Mechanical and Aerospace Engineering.
‡Professor, Mechanical and Aerospace Engineering, xiaolin@seas.ucla.edu, AIAA Associate Fellow.

receptivity process. These weak initial disturbances experience linear growth, leading to nonlinear mode interactions and eventual breakdown. To predict the transition location in path A, current prediction procedures include methods such as the e^N method and the amplitude method by Mack [2]. The widely applied e^N method uses the ratio of the initial amplitude and the maximum amplitude, known as N factor growth rate, to obtain the amplified disturbance amplitude at a particular location. While this method can be easily implemented, various drawbacks exist for improvements. First, this method relies on the validation of LST, which only accounts for the linear growth under the parallel flow assumption. Secondly, this analysis is frequency dependent and does not account for broadband effects. Furthermore, the e^N method does not consider the receptivity mechanism at work. In another word, the e^N method can not predict the generation of instability by external disturbances. The amplitude method, proposed by Mack, provides a better prediction to boundary layer transition due to disturbance by including receptivity, nonlinear, and broadband effects. Integrating across the wavenumber and frequency spectra, this method directly estimates the maximum disturbance amplitude at a given position of the boundary layer with the initial amplitude. Yet, Mack's method can be difficult to implement without assumptions. Marineau [3] made several assumptions to implement the amplitude method in his work. First, since the disturbances have a finite bandwidth, the integration across the frequency spectra can be approximated into a sum. This reduces the required amount of the receptivity data in the spectra. Furthermore, the non-linearity of the breakdown region is estimated with correlations of experimental data. Marineau also attempted to account for the effects of experimental freestream noises. Nevertheless, the receptivity data plays an important role in the amplitude method and the accurate evaluation of receptivity coefficient is necessary.

The receptivity mechanism, which introduces the initial amplitude into the boundary layer for all paths, can include both forced and freestream receptivity. Forced receptivity mechanisms are referred to surface nonuniformities that interact with the boundary layer itself or freestream disturbances, such as the scattering of freestream acoustic waves by a local or distributed surface roughness [4]. Freestream receptivity mechanisms, on the other hand, involve disturbances, such as acoustic waves, vorticity and entropy waves, and turbulent spots, that originate from the freestream flow and interact with the instability waves of the boundary layer [5]. In this chapter, the freestream receptivity, which the external disturbances enter the flow and excite instability, is focused on. During the freestream receptivity process, an energy transfer happens between the disturbance waves and the instability waves in the boundary layer and the such mechanism involved is investigated. Extensive work including theoretical, experimental, and numerical approaches are conducted in the investigation of freestream receptivity. Substantial progress has been made in receptivity studies by the theoretical approach, which includes the use of asymptotic theory alone or in combination with bi-orthogonal decomposition [6] [7] [8] [9]. Yet, the analytical solutions are limited to simple flow geometry and conditions due to the complexity of the analysis. Since the focus of this paper is on the numerical and theoretical analysis, previous studies in the experimental approach will not be reviewed in detail, with an exception of Marineau's experimental work. In his investigation of a Mach 10 boundary layer flow over sharp and blunted cones using the AEDC Hypervelocity Wind Tunnel 9 [10] [11], Marineau observed, for a large bluntness, no significant second mode instability was observed at the start of the transition. In this case, the transition might be linked to tunnel noises or non-modal effects. The latter indicates the need for multimode method in the theoretical analysis for validation. Furthermore, Marineau then implemented the amplitude method in which he evaluated receptivity coefficient by correlating the Reynolds number with the initial amplitude, A_0, of the second mode with the transition wave amplitude from his experimental data [3].

Recently, significant improvements on numerical simulations, such as direct numerical simulation (DNS), can provide detailed insight into the flow physics and allow for the investigation of complex flow configurations. The computational approach also has its own drawbacks such as the cost of computational and the requirement of data analysis [12] [13] [5] [14]. For hypersonic flows, Zhong [12] developed a high-order finite difference (FD) shock-fitting method and later applied this method to study the receptivity of freestream planar acoustic, entropy, and vorticity wave with fixed frequencies for a two dimensional flow over a parabola [15]. Findings from the study showed agreement with the theoretical results which the acoustic disturbance waves are held responsible for the generation of instability waves near the leading edge. Later, Ma and Zhong [13] investigated the receptivity of a Mach 4.5 flow over a flat plate. Ma and Zhong identified discrete modes I, II, and higher that arise from the fast acoustic spectra, and also observed the presence of the 1st, 2nd, and higher modes originating from the slow acoustic spectra. These discrete modes were named the discrete F and S modes accordingly by Fedorov [16] and this nomenclature will be used throughout the remainder of this chapter. In addition to the family of discrete modes, Ma and Zhong also discovered through DNS that although mode F decays, it experiences initial amplitude growth caused by excitation from fast acoustic waves and participates in an inter-modal energy exchange with mode S further downstream, validating the theoretical result by Fedorov [7]. Moreover, the study investigated the effects of different types of freestream disturbances such as acoustic, entropy, and vorticity waves. From each discrete frequency of disturbance implemented, the growth rate and the phase speed of

the perturbation variables can be determined. In the study, the computed phase speed corresponds to the propagation speed of the unstable mode only if the wave is dominated by the unstable mode. When the result contains contributions from different wave modes, the phase speed of a mode will not represented correctly by the computed phase speed. Using this procedure, results revealed that the second mode instability is more receptive to the freestream slow acoustic waves, whereas the fast acoustic waves interact with the decaying mode only. In the case of freestream fast acoustic waves, the discrete mode F interacts directly with the fast acoustic waves, resulting in oscillations in the computed phase speed along the fast acoustic phase speed. This oscillation is the indication of inter-modal energy exchange and a possible solution to extract modal information would be a multi-mode decomposition on the result. The slow acoustic waves directly induce discrete mode S or the Mack modes, which are much stronger than the stable discrete mode F. Furthermore, in his computed growth rate results, an oscillation of growth rate exists near the $-\alpha_i = 0$ line indicating a strong contribution of a neutral, non-decaying boundary layer mode such as the fast acoustic mode. Hence, these observed oscillations in the phase speed and the growth rate do not represent the true phase speed and the growth rate of the dominating unstable mode and a multi-mode analysis such as the bi-orthogonal decomposition would be required for a more accurate prediction of the unstable mode behavior.

Extending the work, Huang and Zhong [17] studied the receptivity due to the interaction between a freestream entropy hotspot of broadband frequencies and the bow shock over a blunt cone and compared simulated results with LST. Since previous studies have been focusing on the receptivity to forcing in discrete frequencies, the broadband effects have been neglected. To study the broadband effects to receptivity, Huang and Zhong utilized a Gaussian shaped pulse as the disturbance pulse to contain a band of frequencies. Similar to the DNS result from Ma and Zhong, the broadband receptivity results exhibits an oscillating behavior of the phase speed near the fast acoustic phase speed indicating significant contribution from the fast acoustic wave in the region near the synchronization point. After the synchronization point, the second mode instability dominates and the oscillation converges to the second mode. The same behavior can be observed in the growth rate as well. Furthermore, Huang and Zhong proposed an approach for obtaining the receptivity coefficient of the second mode.This method approximates the initial amplitude of the dominant mode by dividing the disturbance amplitude at a later location where the unstable mode is dominant with the N factor growth rate. The procedure computes the N factor used in the e^N method with an integration of the spatial growth rate, obtained with LST, from the neutrally stable location s_0 to an arbitrary streamwise location s,

$$N = \int_{s_0}^{s} -\alpha_i \; \mathrm{d}s, \tag{1}$$

where α_i is the computed growth rate. The receptivity coefficient or the initial amplitude is then defined as the ratio between the disturbance amplitude, $A(s, f_n)$, obtained from the unsteady DNS data, and the e^N value,

$$C_{\text{rec}}(f_n) = A_0(f_n) = \frac{A(s, f_n)}{e^{N(s, f_n)}}. \tag{2}$$

Here, the non-dimensional amplitude spectral density, $A(s, f_n)$, is normalized by the freestream pulse density perturbation. This transcribes to a normalized C_{rec} as well. This definition is similar to the receptivity coefficient used in Marineau's work [3] and can be applied in the amplitude method directly. He and Zhong [14], [18], [19], [20] extended further on the broadband receptivity research. They considered the broadband freestream disturbances of various types, including finite and planar acoustic, entropy, and vorticity pulses over a blunt cone of 9.525 mm radius (referred as case B). Here, the planar disturbance corresponds to a pulse infinite in the $y - z$ plane. Similarly, the DNS result obtained by He and Zhong can not be applied directly to compute the receptivity coefficient since various normal modes contribute to the disturbance near the second mode branch I location. Figure 1 shows the phase speed and growth rate results obtained from He which contains oscillations in the region before the second mode domination as a result of multimode contribution.

Following the back tracking method, He was able to compute the second mode initial amplitude and the receptivity coefficient. Consistent with prior research, the receptivity result indicates that the second mode instability being more receptive to a slow acoustic disturbance while the other disturbance types tend to excite unstable frequencies outside of the second mode band. Yet, a direct multimode decomposition at the neutral stability location is necessary to enhance the understanding of receptivity. The receptivity results from He's computation was then applied in the amplitude method implemented by Marineau [3] to improve the accuracy of the transition prediction method. With the numerical results, He was able to generate the receptivity coefficients directly for various flow conditions and scenarios. However, since the method used by He to obtain the receptivity coefficient relies on backtracking to approximate the initial amplitude at the receptivity location, which heavily depends on the N factor, rather than direct calculation, the approach is subject to
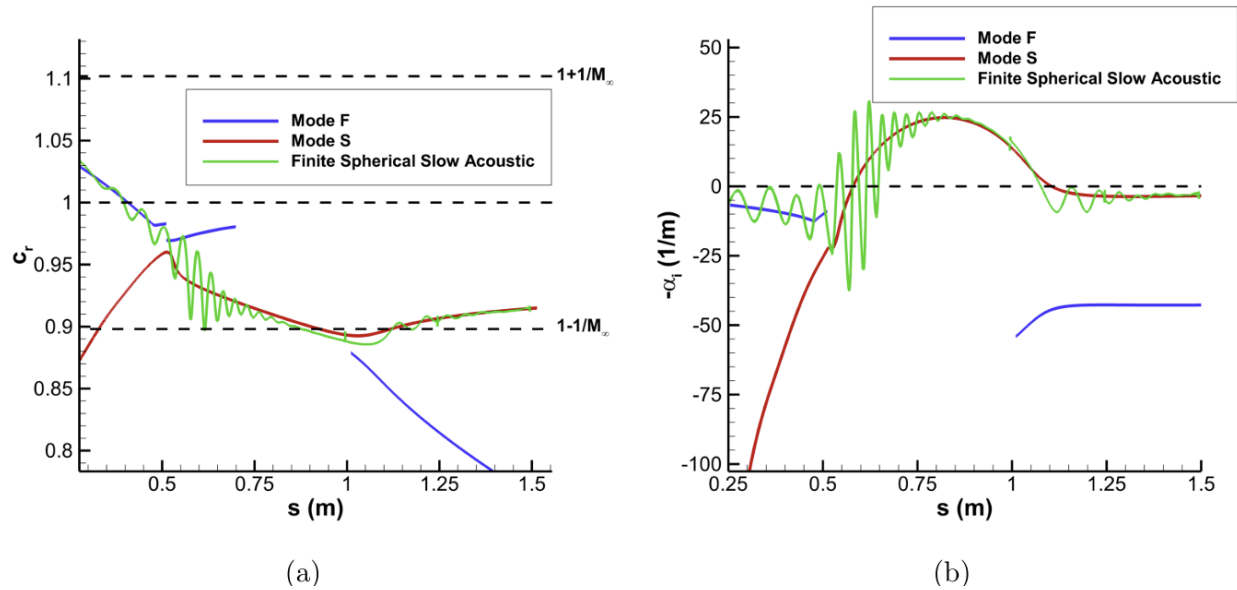
Fig. 1   (a) Phase speed and (b) growth rate obtained with DNS data showing multimode contribution, adopted from He [20]

incorrect assumptions such as non-parallel effects. Furthermore, since at the neutral stability location, modes other than the second mode can contribute to the instability via synchronization and inter-modal energy exchanges, understanding the modal behavior of these other modes by the means of a multimode decomposition would effectively enhance the understanding in receptivity.

The bi-orthogonal decomposition has been proposed as an enhancement to asymptotic and numerical methods for solving the receptivity problem [17] [20]. Proven in the works of Salwen and Grosch [21] and Tumin and Fedorov [22], the solutions to both temporal and spatial problems of linear growth in boundary layer include various normal modes, discrete and continuous. Another set of solutions, which are adjoint and orthogonal to the original problem, exists and forms a bi-orthogonality relationship with the original solution. The BES approach involves using the adjoint fields, which are orthogonal to the original solution, to obtain the amplitude coefficients for each modal solution. In this context, the discrete modes are referred to as two types of waves, referred to as mode F and mode S by Fedorov [16]. The discrete fast mode (mode F) represents a family of high-speed Tollmien-Schlichting (T-S) waves growing in the downstream direction, whereas the second type is made of a family of acoustic waves trapped between the wall and the relative sonic line in the boundary layer. The second mode or discrete slow mode (mode S) is often called the Mack mode as a result of Mack's discovery of this inviscid instability [23]. In addition, the continuous modes are referred to as the non-decaying entropy, vorticity, and fast/slow acoustic waves. These continuous modes originate from the boundary layer and extend to the outer shock layer. The vorticity and entropy modes travel with the phase speed equal to the freestream velocity while the acoustic modes travel at the speed of sound relative to the freestream velocity. Furthermore, the inter-modal energy exchange, known as synchronization, between discrete and continuous modes plays a significant role in the transition. More specifically, the energy exchange between the discrete first mode and second/higher order modes leads to the well-known second mode instability in both computational [13] and theoretical [24] studies.

A survey of applications to receptivity problem in computational and experimental work was presented by Tumin [25]. Saikia et al. [26] used the BES to examine the amplification of the supersonic discrete mode of a high enthalpy flow over a flat plate. Hasnine et al. [27] studied a particulate-induced disturbance over a plate boundary layer of a high-speed flow. Furthermore, the bi-orthogonal eigenfunction system can be modified to include real gas effects. The discrete mode decomposition for a hypersonic reacting gas flow was studied by Ulker [28] and Klentzma [29]. Recently, Luna [30] continued the development of the multimode decomposition of the reacting boundary layer to obtain the bi-orthogonal eigenfunction system, including both discrete and continuous modes, for a hypersonic flow over a flat plate. However, in the work mentioned above, the bi-orthogonal eigenfunction system was formulated into an initial value problem and computed with an integration-based method. This initial value problem approach, while offering a

4

local solution with individual eigenmode computation, contrasts with Zou and Zhong's method [31], which solves the BES as a boundary value problem. Zou and Zhong's approach allows for both global and local methods and is more suited to high-order finite difference computations.

The primary goal of this paper is to demonstrate a direct and accurate evaluation of the initial disturbance amplitude at the branch I neutral stability point by deploying bi-orthogonal decomposition. Implementing the high-order finite difference method used by Zou [31], the bi-orthogonal eigenfunction system for a hypersonic flow over a blunt cone including discrete and continuous acoustic modes is obtained. Preliminary result of the receptivity flow field decomposition has shown agreement between the decomposed mode S amplitude and the back-traced mode S amplitude based on the e^N method. With the initial amplitudes obtained with the bi-orthogonal decomposition, the receptivity coefficient can be computed to further improve the amplitude method in transition prediction. Furthermore, an additional discrete mode, in addition to the discrete F and S modes, is found with behavior aligning with an entropy layer mode. The influence of such disturbance on the transition is limited and needs further investigation.

II. Governing Equations

A. Navier-Stokes equations

The Navier-Stokes equations for a viscous compressible flow of ideal gas in Cartesian Coordinates are

$$\frac{\partial \rho^*}{\partial t^*} = \nabla^* \cdot (\rho^* \mathbf{u}^*) = 0 \tag{3}$$

$$\rho^* \left[\frac{\partial \mathbf{u}^*}{\partial t^*} + (\mathbf{u}^* \cdot \nabla^*) \mathbf{u}^* \right] = -\nabla^* p^* + \nabla^* \cdot \left[\lambda^* (\nabla^* \cdot u^*) \mathbf{I} + \mu^* \left(\nabla^* \mathbf{u}^* + \nabla^* \mathbf{u}^{*T} \right) \right] \tag{4}$$

$$\rho^* c_p^* \left[\frac{\partial T^*}{\partial t^*} + (\mathbf{u}^* \cdot \nabla^*) T^* \right] = -\nabla^* \cdot (\kappa^* \nabla^* T^*) + \frac{\partial p^*}{\partial t^*} + \mathbf{u}^* \cdot \nabla^* p^* + \Phi^* \tag{5}$$

where viscous dissipation function is

$$\Phi^* = \lambda^* (\nabla^* \cdot \mathbf{u}^*)^2 + \frac{\mu^*}{2} \left[\nabla^* \mathbf{u}^* + \nabla^* \mathbf{u}^{*T} \right]^2. \tag{6}$$

The ideal gas law is expressed as

$$p^* = \rho^* R^* T^*. \tag{7}$$

In the above equations, the asterisk, $*$, represents the dimensional form of the variables. The coefficients, c_p is the specific heat and κ is the heat conductivity. We also make use of the Stokes' hypothesis of $\lambda^* = -2\mu^*/3$. The viscosity μ is given by the Sutherland formula.

$$\mu = \mu_{ref} \left(\frac{T}{T_{ref}} \right)^{3/2} \frac{T_{ref} + S_\mu}{T + S_\mu}. \tag{8}$$

The thermal conductivity k is also formulated by the Sutherland formula with the Sutherland temperature S_k.

B. Linear Stability Theory

To study the property of instability waves in the boundary layer flow, a small perturbation is assumed. From the Navier-Stokes equations, we can derive the stability equations by assuming a small disturbance added on to the flow variables,

$$\text{For small disturbances:} \quad \begin{array}{lll} u = \bar{U} + \tilde{u}, & v = \bar{V} + \tilde{v}, & w = \bar{W} + \tilde{w} \\ p = \bar{P} + \tilde{p}, & \tau = \bar{T} + \tilde{\theta}, & \rho = \bar{\rho} + \tilde{\rho} \\ \mu = \bar{\mu} + \tilde{\mu} & k = \bar{k} + \tilde{k}. \end{array} \tag{9}$$

where the disturbance variable is small comparing to the mean variables, for example, $\tilde{u} \ll \bar{U}$. Here, the "bar" quantities represent the meanflow variables and the "bar" symbol is dropped in the following text. For the compressible boundary

layer flow, all flow variables are non-dimensionalized by their corresponding boundary layer edge values, velocities by u_e, pressure by $\rho_e u_e^2$, density by ρ_e. A reference length scale L is assumed for all lengths and the time variable, t, is scaled by l/u_e. The quasi-parallel assumption, which assumes the mean variable dependence is on the wall normal direction such as, $U \approx U(y)$ and $V = 0$, is applied. By neglecting the higher order terms such as $\tilde{u}^2$ and subtracting the meanflow equations, we can obtain the non-dimensional linear stability equations. For a flat plate profile, the assumption of $dP/dy \to 0$ causes the pressure profile to be constant, $P = 1/\gamma M^2$. For meanflow profiles of other geometry, as suggested by Miselis [32], the assumption is not applicable and the meanflow pressure distribution has to be accounted for in the linearized equations. The meanflow velocity boundary condition at the wall will be the no slip condition. The meanflow temperature boundary condition can be adiabatic or isothermal at the wall

$$U_{wall} = 0$$
$$\frac{dT_{wall}}{dy} = 0 \text{ or } T_{wall} = \text{constant} \tag{10}$$

For the fluctuations, the velocity at the wall will still have the no slip condition. However, the fluctuation temperature boundary condition is set to be zero because of the thermal inertia of the wall.

$$\tilde{u}_{wall}, \tilde{v}_{wall}, \tilde{w}_{wall} = 0$$
$$\tilde{\theta} = 0 \tag{11}$$

In the freestream, the meanflow is uniform for a flow over a flat plate while the freestream meanflow is determined by the shock using the Rankine- Hugoniot condition in the DNS [12]. The freestream perturbations are bounded allowing the existence of neutral continuous modes [21],

$$y \to \infty : \left| \tilde{u}, \tilde{v}, \tilde{w}, \tilde{p}, \tilde{\theta} \right| < \infty, \tag{12}$$

as well as the corresponding spatial derivatives in the streamwise and spanwise direction.

From the set of linear stability equations, a periodic-in-time perturbation is assumed, which leads to a solution in form of $\exp(-i\omega t)$ after a Fourier transformation in time is performed. After the transformation, the perturbation variables and their corresponding spatial derivatives are defined in a column vector, A, with 16 components,

$$\mathbf{A}(x, y, z) = (u, \partial u/\partial y, v, p, \theta, \partial\theta/\partial y, w, \partial w/\partial y, \partial u/\partial x, \partial v/\partial x$$
$$\partial\theta/\partial x, \partial w/\partial x, \partial u/\partial z, \partial v/\partial z, \partial\theta/\partial z, \partial w/\partial z)^T. \tag{13}$$

The $\hat{u}$ notation is dropped and written as u for simplicity in notation. Following Tumin [33], the linearized Navier-Stokes system is rewritten in the following matrix form. Again, the wall boundary conditions are no slip velocity and zero temperature perturbation while the freestream boundary condition is a bounded condition because of the existence of neutral oscillating modes.

$$\frac{\partial}{\partial y}\left(\mathbf{L}_0 \frac{\partial \mathbf{A}}{\partial y}\right) + \mathbf{L}_1 \frac{\partial \mathbf{A}}{\partial y} = \mathbf{H}_1 A + \mathbf{H}_2 \frac{\partial \mathbf{A}}{\partial x} + \mathbf{H}_3 \frac{\partial \mathbf{A}}{\partial z}$$
$$y = 0 : u = v = w = \theta = 0,$$
$$y \to \infty : |(\mathbf{A})_i| < \infty, \quad i = 1, \dots, 16, \tag{14}$$

where the subscript i denotes the ith component of the vector $\mathbf{A}(y)$ at a y location. The matrices $\mathbf{L}_0$, $\mathbf{L}_1$, $\mathbf{H}_1$, $\mathbf{H}_2$, and $\mathbf{H}_3$ are 16 by 16 matrices of coefficients with their components shown in Appendix. In this study, the perturbation is assumed to take form of a travelling wave, such as the following streamwise velocity disturbance variable, $\tilde{u}$,

$$\tilde{u} = \hat{u}(y) \exp[i(\alpha x + \beta z - \omega t)] \tag{15}$$

where α and β are the streamwise and spanwise wave numbers, c is the wave propagation speed, and $\omega = \alpha c$ is the wave frequency. The wave shapefunction is denoted by $\hat{u}(y)$. In the temporal problem, both wavenumbers, α and β are assumed real and the complex frequency ω is determined. On the other hand, for the spatial problem, the spanwise wave number β and the frequency ω are real valued and the streamwise wavenumber α is complex. For discrete modes, the streamwise wavenumber α is solved as a complex eigenvalue. For continuous modes, however, the streamwise wavenumber α is determined from the branch cuts in the solution of the Cauchy problem presented in the later section. Substituting the solution form of Eq.(15) into the linear stability equations of Eq. (14) and eliminating the

$\exp[i(\alpha x + \beta z - \omega t)]$ on both sides of the equation, the system with $\mathbf{A}_{\alpha\beta}$ being the transformed variable of $\mathbf{A}$ in Eq. (13) can be written as

$$\frac{\partial}{\partial y}\left(\mathbf{L}_0\frac{\partial \mathbf{A}_{\alpha\beta}}{\partial y}\right) + \mathbf{L}_1\frac{\partial \mathbf{A}_{\alpha\beta}}{\partial y} = \mathbf{H}_1\mathbf{A}_{\alpha\beta} + i\alpha\mathbf{H}_2\mathbf{A}_{\alpha\beta} + i\beta\mathbf{H}_3\mathbf{A}_{\alpha\beta}$$

$$y = 0: \quad (\mathbf{Z}_{\alpha\beta})_i = 0, \quad i = 1, 3, 5, 7$$

$$y \to \infty: \quad \left|(\mathbf{A}_{\alpha\beta})_i\right| < \infty, \quad i = 1, \ldots, 16. \tag{16}$$

where the boundary conditions of Eq. (14) are also transformed into the boundary conditions in Eq. (16). The elements of $\mathbf{L}_0$, $\mathbf{L}_1$, $\mathbf{H}_1$, $\mathbf{H}_2$, and $\mathbf{H}_3$ are given in Appendix. For implementation, Eq. (16) can be recast as a first-order system of eight components of the following with the corresponding boundary conditions,

$$\frac{d\mathbf{z}_{\alpha\beta}}{dy} = \mathbf{H}_0\mathbf{z}_{\alpha\beta}$$

$$y = 0: (\mathbf{z}_{\alpha\beta})_i = 0, \quad i = 1, 3, 5, 7$$

$$y \to \infty: \left|(\mathbf{z}_{\alpha\beta})_i\right| < \infty, \quad i = 1, \ldots, 8, \tag{17}$$

with $\mathbf{z}_{\alpha\beta}$ defined as

$$\mathbf{z}_{\alpha\beta} = (u, \partial u/\partial y, v, p, \theta, \partial \theta/\partial y, w, \partial w/\partial y). \tag{18}$$

Here, $\mathbf{H}_0$ is a 8 by 8 coefficient matrix. The elements of $\mathbf{H}_0$ can be found in Appendix A. The solutions of Eq. (17) can be classified into two types, discrete and continuous modes, according to the freestream boundary conditions. For the condition at the freestream, the boundedness condition allows for the existence of neutral waves oscillating outside of the boundary layer known as continuous modes. For the discrete modes, on the other hand, the freestream boundary condition is limited to the decaying behavior only. The two types of solutions combine to form a complete set of solutions as a superposition of discrete and continuous eigenfunctions accordingly,

$$\mathbf{A} = \sum_n C_n\mathbf{A}_{\alpha_n}(y)e^{i\alpha_n x} + \sum_j \int_0^\infty C_j\mathbf{A}_{\alpha_j}(y)e^{i\alpha_j(k)x}dk. \tag{19}$$

with $A_{\alpha n}$ representing the discrete modes and $A_{\alpha j}$ being the continuous modes, containing a superposition of the fundamental solution $\mathbf{U}$. Since any perturbation can be decomposed into discrete and continuous modes, the bi-orthogonal decomposition procedure can be formulated. The numerical implementation to obtain both discrete and continuous modes using finite difference method will be discussed in Section III.

C. Adjoint Problem and Bi-orthogonal Eigenfuncion System

Let the operator $\mathcal{L}$ be the linear operator of the direct spatial problem from Eq. (16). We can introduce the general adjoint operator $\mathcal{L}^\dagger$ from the inner product of a general vector $\mathcal{L}\mathbf{X}$ and $\mathbf{Y}$.

$$\langle\mathcal{L}\mathbf{X}, \mathbf{Y}\rangle = \langle\mathbf{X}, \mathcal{L}^\dagger\mathbf{Y}\rangle. \tag{20}$$

where $\mathbf{Y}$ is the set of eigenvectors for the adjoint operator $\mathcal{L}^\dagger$. Here, the inner product is defined on the range of $[a, b]$ as

$$\langle\mathbf{X}, \mathbf{Y}\rangle = \int_a^b \mathbf{X}(y)\mathbf{Y}(y)dy, \tag{21}$$

Here, the inner product is without the complex conjugate since the complex conjugate will be introduced in the definition of the adjooint solutions later. Now, let $\mathbf{A}_{\alpha\beta}$ of Eq. (16) equal to $\mathbf{X}$ of the adjoint definition in Eq. (20). With the same assumptions and corresponding boundary conditions, the following adjoint system with $\mathbf{B}_{\alpha\beta} = \overline{\mathbf{Y}}$, where the overbar notation denotes the complex conjugate, from Eq. (21) can be introduced,

$$\frac{\partial}{\partial y}\left(\mathbf{L}_0^T\frac{\partial \mathbf{B}_{\alpha\beta}}{\partial y}\right) - \mathbf{L}_1^T\frac{\partial \mathbf{B}_{\alpha\beta}}{\partial y} = \mathbf{H}_1^T\mathbf{B}_{\alpha\beta} + i\alpha\mathbf{H}_2^T\mathbf{B}_{\alpha\beta} + i\beta\mathbf{H}_3^T\mathbf{B}_{\alpha\beta}$$

$$y = 0: \quad (B_{\alpha\beta})_i = 0, \quad i = 2, 4, 6, 8$$

$$y \to \infty: \quad \left|(B_{\alpha\beta})_i\right| < \infty, \quad i = 1, \ldots, 16. \tag{22}$$

7

Here, the transpose is the conventional transpose without conjugation since the complex conjugate is introduced in the definition of $\mathbf{B}_{\alpha\beta}$. The boundary conditions for the adjoint problems are also obtained from the inner product definition with the direct problem boundary conditions. The adjoint system can also be recast in the following form of first order equations, with $\mathbf{Y}_{\alpha\beta}$ being the solution across the entire boundary layer,

$$
\begin{aligned}
-\frac{\mathrm{d}\mathbf{Y}_{\alpha\beta}}{\mathrm{d}y} &= H_0^T \mathbf{Y}_{\alpha\beta}. \\
y = 0: \quad &(Y_{\alpha\beta})_i = 0, \quad i = 2, 4, 6, 8 \\
y \to \infty: \quad &\left|(Y_{\alpha\beta})_i\right| < \infty, \quad i = 1, \ldots, 8
\end{aligned}
\tag{23}
$$

The transformation between $\mathbf{B}_{\alpha\beta}$ and $\mathbf{Y}_{\alpha\beta}$ can be referred to Tumin [33]. With the dual systems, the orthogonality condition exists as

$$
i\left(\alpha - \alpha'\right) \int_0^\infty \left(\mathbf{H}_2 \mathbf{A}_{\alpha\beta}, \mathbf{B}_{\alpha'\beta}\right) dy = 0.
\tag{24}
$$

This orthogonality relation can be obtained by an integration by part of the dot product between $\mathbf{B}_{\alpha'\beta}$ and Eq. (16). The above equation can be rewritten into this form,

$$
\left\langle \mathbf{H}_2 \mathbf{A}_{\alpha\beta}, \mathbf{B}_{\alpha'\beta} \right\rangle = \int_0^\infty \left(\left(\mathbf{H}_2 \mathbf{A}_{\alpha\beta}\right), \mathbf{B}_{\alpha'\beta}\right) dy = \Gamma \Delta_{\alpha\alpha'}.
\tag{25}
$$

According to [21], for the discrete modes , the term $\Delta_{\alpha\alpha'}$ represents a Kronecker Delta, which equals to 1 if the eigenvalues of the two modes are the same. This is because the decaying behavior of the discrete modes and the integral should result in a constant Γ value depending on the normalization. For the continuous modes, the same term represents a Dirac Delta. One can also derive the following inner product relation between $\mathbf{A}_{\alpha\beta}$ and $z_{\alpha\beta}$. This would be helpful in the numerical implementation [33],

$$
\left\langle H_2 \boldsymbol{A}_{\alpha\beta}, \boldsymbol{B}_{\alpha\beta} \right\rangle = -\mathrm{i} \left\langle \frac{\partial \boldsymbol{H}_0}{\partial \alpha} z_{\alpha\beta}, \boldsymbol{Y}_{\alpha\beta} \right\rangle.
\tag{26}
$$

To verify the bi-orthogonality of the modes, the orthogonality relationship is evaluated numerically in the later section. Subsequently, the coefficients for each modes can be obtained using the following relation assuming local parallel flow,

$$
C_{mode} = \frac{-\mathrm{i} \left\langle \frac{\partial \boldsymbol{H}_0}{\partial \alpha} z_{DNS}, \boldsymbol{Y}_{\alpha\beta} \right\rangle}{\Gamma}.
\tag{27}
$$

III. Numerical Methods

A. Discrete and Continuous Modes

The general high-order finite difference method on a non-uniform grid by Zou [31] is applied to obtain the discrete and continuous modes. The domain in wall normal direction is non-uniform enabling a direct dicretization. The distribution of N number of grid points over the domain $[a, b]$ will follow Kosloff [34], Zhong [35], and Shukla [36],

$$
y_j = \frac{b+a}{2} + (b-a)\frac{\sin^{-1}(-\alpha_g \cos(\pi j/N))}{2\sin^{-1}\alpha}, \quad j = 0, \ldots, N.
\tag{28}
$$

where $a = 0$ and $b = y_\infty$. In Eq. (28), α_g refers to the grid stretching parameter and does not relate to the streamwise wavenumber mentioned in other parts of the paper. The grid stretching parameter, α_g is set to be 0.9995 to ensure stability [35]. Let the operator D be the discrete difference operator obtained using the high-order finite difference method by Zou [31], along with boundary conditions, Eq. (17) can be written as

$$
\begin{aligned}
\left(\mathbf{D} - \left(\mathbf{A} + \alpha\mathbf{B} + \alpha^2\mathbf{C}\right)\right) \mathbf{z}_{\alpha\beta} &= 0 \\
y = 0: (\mathbf{z}_{\alpha\beta})_i, \quad &j = 1, 3, 5, 7 \\
y = y(N): \left|(\mathbf{z}_{\alpha\beta})_i\right| < \infty, \quad &i = N*8, \ldots, N*8 - 7.
\end{aligned}
\tag{29}
$$

where $(\mathbf{z}_{\alpha\beta})_i$ is the ith component of the discrete vector $\mathbf{z}_{\alpha\beta}$ of length $N \times 8$. The problem can then be described as a set of linear equations taking form in $[\mathbf{A}][\mathbf{x}] = [\mathbf{b}]$, where $[\mathbf{A}] = [\mathbf{D} - (\mathbf{A} + \alpha\mathbf{B} + \alpha^2\mathbf{C})]$, $[\mathbf{x}] = [\mathbf{z}_{\alpha\beta}]$, and $[\mathbf{b}] = 0$.

8

Note that Eq. (29) has a nonlinear dependence on the spatial wavenumber α. If the nonlinear term is omitted or α^2 is set to 0, a global eigenvalue decomposition can be performed. The discrete adjoint operators can be obtained in the same way. Following Eqs. (23), the discrete adjoint formula can be written as

$$
\begin{aligned}
-\mathbf{DY}_{\alpha\beta} - \mathbf{H}^T\mathbf{Y}_{\alpha\beta} &= 0 \\
y = 0 : (\mathbf{Y}_{\alpha\beta})_i &= 0, \quad i = 2, 4, 6, 8 \\
y = y(N) : \left|(\mathbf{Y}_{\alpha\beta})_i\right| &< \infty, \quad i = N*8, \ldots, N*8-7.
\end{aligned}
\tag{30}
$$

For the implementation of boundary conditions, Zou and Zhong presented a detailed formulation and implementation procedure for both discrete and continuous modes [31]. With the discrete system, the sparse LU decomposition from MATLAB is used to solve the linear system. With the discrete and continuous modes computed, the bi-orthogonal decomposition method to obtain receptivity coefficients is described.

B. DNS

With the goal to perform the bi-orthogonal decomposition for the hypersonic receptivity flow over a flat plate, both the steady and unsteady flow field are required. The meanflow profile is obtained with the flat plate boundary layer flow formulation from Malik [37] and a shooting method while the unsteady flow field will be obtained by DNS. A receptivity simulation is performed with a high-order shock-fitting direct numerical simulation developed by Zhong [12] for a hypersonic flow over a flat plate . In the DNS code, the conservative Navier Stokes equations are transformed into a computational space with the coordinates (ξ, η, ζ). The physical domain is described by a curvilinear grid that matches the geometry. From Zhong, the shock is treated as a moving boundary and the flow condition behind the shock is determined with the Rankine-Hugoniot relations. The numerical scheme used is a fifth order upwind scheme for the inviscid fluxes and a sixth order central scheme for the viscous fluxes. Additional details of the general numerical method used for the DNS simulation and the shock-fitting scheme can be found in Zhong [12]. For steady meanflow, a parallel assumption is applied such that the meanflow variables are functions of the wall normal direction coordinate only. Under this assumption, the flow field data is divided into wall normal snapshots for each streamwise location and each snapshot at these streamwise sampling locations is analyzed.

For the unsteady receptivity simulation, the perturbed flow field is obtained by imposing a propagating Gaussian distribution freestream disturbance throughout the domain.

$$
q(x, y, z, t) = |q'|_\infty \exp\left(-\frac{(R_c)^2}{2\sigma^2}\right) + q_\infty.
\tag{31}
$$

The term q is the disturbance variable and $|q'|_\infty$ stands for the peak freestream perturbation. The term R_c refers to the radial distance from the center of the pulse to a point in the flow field. The variable σ controls both the spatial width of the pulse as well as the frequency bandwidth of the disturbance. To study the receptivity behavior to various disturbances, the perturbed flow field resulting from each pulse is decomposed into their spectral frequency components. The unsteady DNS flow field is analyzed with Fourier Transform to obtain the disturbance information in the discrete frequency spectrum. The Fast Fourier Transform (FFT),

$$
h(t_k) \equiv h_k \approx \sum_{n=0}^{N-1} H(f_n) e^{-2\pi i f_n t_k},
\tag{32}
$$

is used to transform all the time dependent perturbation variables, u, p, v, ρ. The perturbation variables are inputted as $h(t_k)$ and outputted as the complex coefficient $H(f_n)$ for the n_{th} frequency in a total of N discrete frequencies. With the amplitude of the disturbance, the DNS local growth rate can be computed as

$$
-\alpha_i = \frac{1}{|H(f_n)|} \frac{d|H(f_n)|}{ds}
\tag{33}
$$

where s is the streamwise coordinate starting from the nose of the cone. Figure (b) 1 shows the growth rate computed with the local unsteady surface pressure amplitudes. The oscillations are attributed to the multimode influences in existing literature [17] [14] [20]. To recover the LST growth rate of a particular mode, the bi-orthogonal decomposition is deployed to obtain the modal amplitude for the evaluation of Eq. (33).

9

C. Bi-orthogonal Decomposition for Receptivity

Taking the newly formulated solutions as orthogonal modes, any perturbation can be written as a combination of discrete and continuous modes from Eq. (19). Let us consider a decomposition of the computational data $\mathbf{A}_D$ with the discrete modes and the continuous modes. The components of $\mathbf{A}_D$ are the spectral components of the perturbation variables for a given frequency, f, arranged in the order defined in Eq. (13). These perturbation variables can be obtained from the numerical result of DNS. For experiments, Tumin also showed an example of the bi-orthogonal decomposition using limited data from measurement [38]. Eq. (19) of any perturbation can be expressed as follows, where $P = 2$ represents the number of discrete modes (F and S), and $Q = 5$ represents the number of continuous modes (fast and slow acoustic modes, two vorticity modes, and entropy mode).

$$\mathbf{A}_D(x, y, f) \approx \sum_n^P C_n \mathbf{A}_{\alpha\beta_n}(y) e^{i\alpha_n x} + \sum_j^Q \int_0^\infty C_j \mathbf{A}_{\alpha\beta_j}(y) e^{i\alpha_j(k)x} dk. \tag{34}$$

where C_n corresponds the modal coefficient of the nth discrete mode and $\mathbf{A}_{\alpha\beta_n}(y)$ being the discrete mode eigenfunction. The coefficients C_j refers to the coefficient of the jth continuous mode and $\mathbf{A}_{\alpha\beta_j}(y)$ is the corresponding wave shapefunction. Let the vector $\mathbf{z}_D$ be the first eight components of $\mathbf{A}_D$, the coefficients for each mode can be obtained with Eq. (27). The modal coefficient, C_m, where $m = n$ for the nth discrete mode and $m = j$ for the jth continuous mode, is as follow

$$C_m = \frac{\left\langle \frac{\partial \boldsymbol{H}_0}{\partial \alpha} \mathbf{z}_D, \mathbf{Y}_{\alpha\beta}^m \right\rangle}{\left\langle \frac{\partial \boldsymbol{H}_0}{\partial \alpha} \mathbf{z}_{\alpha\beta}^m, \mathbf{Y}_{\alpha\beta}^m \right\rangle}. \tag{35}$$

With $\mathbf{z}_{\alpha\beta}^m$ being the direct eigenfunction of the nth discrete mode or the jth continuous mode from Eq. (34) and $\mathbf{Y}_{\alpha\beta}^m$ being the adjoint eigenfunction obtained from from Eq. (23) for the corresponding discrete or continuous mode. In practice, the inner products from Eq. (35) can be written as

$$\left\langle \frac{\partial \boldsymbol{H}_0}{\partial \alpha} \mathbf{z}_\mathbf{D}, \mathbf{Y}_{\alpha\beta}^m \right\rangle = \int_0^\infty \left(\frac{\partial \boldsymbol{H}_0}{\partial \alpha} \mathbf{z}_\mathbf{D}, \mathbf{Y}_{\alpha\beta}^m \right) dy, \tag{36}$$

and

$$\left\langle \frac{\partial \boldsymbol{H}_0}{\partial \alpha} \mathbf{z}_{\alpha\beta}^\mathbf{m}, \mathbf{Y}_{\alpha\beta}^m \right\rangle = \int_0^\infty \left(\frac{\partial \boldsymbol{H}_0}{\partial \alpha} \mathbf{z}_{\alpha\beta}^\mathbf{m}, \mathbf{Y}_{\alpha\beta}^m \right) dy. \tag{37}$$

Using a non-uniform trapezoidal rule, the integration can be numerically implemented as the following. Let f be the function of the dot product inside the integral for Eq. (37),

$$\int_0^\infty f dy \approx \sum_{k=1}^N \frac{f(y_{k-1}) + f(y_k)}{2} \Delta y_k, \tag{38}$$

where ∞ is approximated at the freestream upper bound y_{max} location of the domain. Note that a consistent normalization across the modes is necessary as the normalization is dependent on the normalization boundary conditions mentioned above.

For each continuous branch, The integral in Eq. (34) can be approximated with a Riemann sum or other numerical integration scheme over the discrete branch parameter k_l, $l = 1, \cdots, N$ for N discrete points in the range of k. For the jth mode, the corresponding branch can be approximated as

$$\int_0^\infty C_j \mathbf{A}_{\alpha_j}(y) e^{i\alpha\beta_j(k)x} dk \approx \sum_l^N C_j(k_l) \mathbf{A}_{\alpha\beta_j}(y, k_l) e^{i\alpha_j(k)x} \Delta k. \tag{39}$$

For every discrete branch parameter of k, the continuous mode coefficient, $C_j(k)$, and the continuous mode functions, $\mathbf{A}_{\alpha\beta_j}(k)$, from Eq. (39) need to be computed and summed in order to account for the contribution of the whole branch. Substituting Eq. (39) into Eq. (34), the numerical result from DNS can be approximated as

$$\mathbf{A}_D(x, y, f) \approx \sum_n^P C_n \mathbf{A}_{\alpha\beta_n}(y) e^{i\alpha_n x} + \sum_j^Q \sum_l^N C_j(k_l) \mathbf{A}_{\alpha\beta_j}(y, k_l) e^{i\alpha_j(k_l)x} \Delta k. \tag{40}$$

10

Utilizing the bi-orthogonal decomposition shown above, the individual amplitude of perturbation variables can be obtained for each mode and the result can be used to aid receptivity studies, particularly in the computation of receptivity coefficient.

Since the role of receptivity coefficient in the amplitude method is significant to the prediction of transition location [2] [3], an accurate computation to obtain the receptivity coefficient is essential. Theoretically, the receptivity coefficient is defined as the ratio of initial perturbation amplitude of the unstable mode, A_I, where the subscript I corresponds to the data measured at the branch I location of the neutral stability curve given a frequency, over the freestream disturbance amplitude, A_∞, in the works of Marineau [3] and He and Zhong [14], given by

$$C_\mathrm{rec} = \frac{A_\mathrm{I}}{A_\infty} \tag{41}$$

where A_I is the unstable mode amplitude of a perturbation variable, which can be u, v, p, θ, in the vector $\mathbf{A}$ from Eq. (13), for a specific frequency ω. This amplitude A_I contains both magnitude and phase angle. Most applications using the initial amplitude, such as the computation of receptivity coefficient, only require the magnitude of A_I. In DNS studies, the phase angle is also significant to the simulation result [14]. The pressure component at the wall p_wall, which is 4th component of $\mathbf{A}$ at $y = 0$, is used by He and Zhong as A_I in his cases while the freestream pulse density perturbation of the same frequency is used for A_∞ in Eq. (41) [14].

To obtain the initial amplitudes of the unstable mode at the branch I location, the bi-orthogonal decomposition described is applied. Using the mth mode amplitude coefficient of C_m from Eq. (27) and the solution of the corresponding mode, $\mathbf{z}^m_{\alpha\beta}$ or $\mathbf{A}^m_{\alpha\beta}$, evaluated at the branch I location, the receptivity coefficient of the mth discrete or continuous mode for the mth mode can be formulated as

$$C_\mathrm{rec} = \frac{C_m \mathbf{A}^m_{\alpha\beta}(y = 0)}{A_\infty} = \frac{C_m \mathbf{z}^m_{\alpha\beta}(y = 0)}{A_\infty} \tag{42}$$

Note that the bi-orthogonal eigenfunctions formulated above are normalized by the wall pressure. Thus, $C_m \mathbf{A}^m_{\alpha\beta}(y = 0)$ is multiplied by the wall pressure amplitude obtained by DNS to recover the absolute amplitude at the wall. The above presents the procedure of obtaining the receptivity coefficient of an unstable mode by bi-orthogonal decomposition. A case of receptivity analysis for a hypersonic flow over a blunt nose cone will be discussed in the later section.

IV. Results

A. Decomposition for Mode S

In this section, the numerical result of mode S amplitude obtained from the bi-orthogonal decomposition over various streamwise locations for a hypersonic flow over a blunt cone subject to an acoustic pulse is presented. The flow conditions are presented in Table 1.

Table 1   Freestream Conditions of hypersonic flow over a blunt nose cone following He [14].

R_n(mm)	M_∞	$h_{0,\infty}$(MJ/kg)	ρ_∞ (kg/m^3)	p_∞(kPa)	T_∞(K)	U_∞(m/s)	$T_w/T_{0,\infty}$	Pr
5.080	9.81	1.06	0.0422	0.64	50.8	1425	0.3	0.72

With the flow parameters shown in Table. 1, Fig. 2 shows the meanflow contours of Mach number, pressure, and temperature. From Fig. 2a, the boundary layer development can be observed near the wall. Furthermore, the shock layer was converged with the shock as the upper boundary through the Rankine-Hugoniot relations. The meanflow pressure near the nose region is shown in Fig. 2b, normalized by the freestream value. The pressure contour indicates that the pressure throughout the shock layer is nearly constant downstream from the centerline distance $X = 0.01$ m, which is relatively upstream compared to the full domain length of 1.5 m. Moreover, the temperature contour in Fig. 2c depicts an entropy layer being present and extending downstream. This entropy layer is associated with the transition reversal process observed in nose bluntness studies [39] [40]. Before the reversal, the increasing nose bluntness reduces the local Reynolds number and delays the transition. However, when the nose bluntness exceeds a critical value, this reduction is reversed with no significant contribution from the second-mode instability waves [40], suggesting other forms of excitation. Traditionally, the existence of entropy-layer instabilities observed by Stetson at low frequencies was

11

identified with small amplification rates [41]. Yet, Another type of entropy-layer disturbance was found by Dietz and Hein located at a second generalized inflection point outside the boundary-layer edge [42]. Wan, Su, and Chen [43] further concluded with the comparison between DNS and LST that this entropy-layer disturbance is dominant after the first mode decay and further induces instability when the entropy layer is swallowed by the developing boundary layer. Subsequently, this entropy-layer instability is identified as an entropy-layer mode [44]. The bi-orthogonal decomposition at the second mode branch I neutral stability location in the later section also indicates that an higher order discrete mode other than mode S contributes to the entropy layer disturbance.

(a) Mach number contour. (b) Pressure contour. (c) Temperature contour.
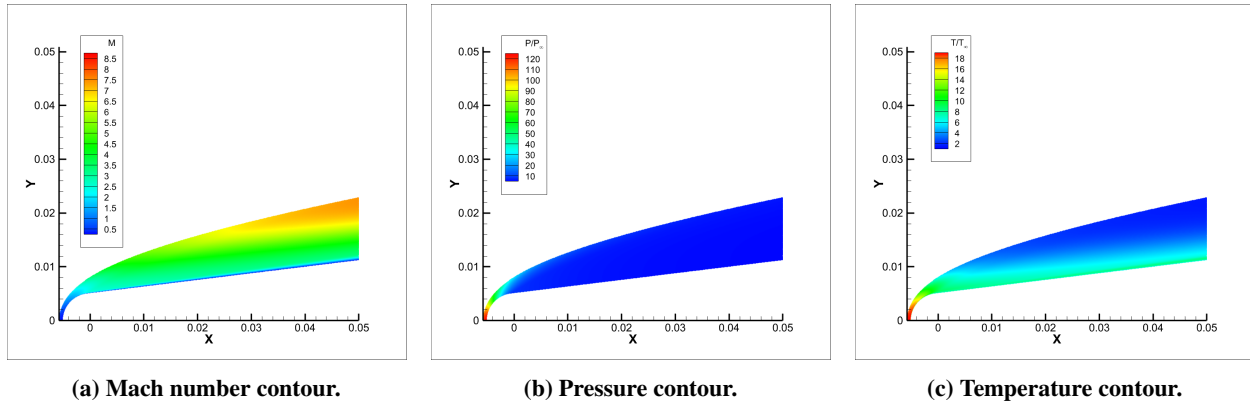
Fig. 2   a) Mach number, b) Normalized pressure, and c) Normalized temperature contour near the blunt nose region. Note that the full domain of the cone ends at the central line distance of $X = 1.5$ m.

Subsequently, the unsteady simulation is performed to obtain the perturbed flowfield for bi-orthogonal decomposition. This unsteady simulation introduces a freestream pulse in front of the blunt nose and the flowfield is recorded as the pulse propagates downstream. The finite spherical pulse parameters and schematic setup are provided in [19] and [14], referred to as Case I. The slow acoustic disturbance in the freestream has a peak density perturbation amplitude, $|\rho'|_\infty$, of 1×10^{-6} as well as a peak pressure perturbation amplitude $|P'|_\infty = |\rho'|_\infty \gamma$. The parameter σ for the finite spherical pulse is set to 1×10^{-3}. The pulse is set to start the advection at a location $x_0 = -0.02$ m with a slow acoustic disturbance speed of $c_\infty = u_\infty - a_\infty$. Temporal snapshots of the unsteady flowfield at various streamwise locations are transformed by using FFT to obtain the spectral components for the bi-orthogonal decomposition. Utilizing the FFT perturbation data at a particular frequency, a projection onto the discrete and continuous modes can be performed, enabling a comprehensive analysis of the flowfield's modal composition.

To validate the accuracy of the decomposition result, the amplitude of $C_s A_s$ is plotted against the backtracked amplitude $|A| = |A(s^*, f_n)/e^{N(s^*, f_n)}|$ where $N = \int_s^{s^*} -\alpha_i ds'$ and s^* is a downstream second mode dominant location in Fig. 3. Here, C_s is the modal coefficient from the bi-orthogonal decomposition, used to only account for the mode S amplitude. In this comparison, the downstream location of $s* = 1$m is regarded as second-mode dominant. This can be observed from Fig. 1 where the DNS result aligns with the LST growth rate for mode S. The branch I location is located at $s^* = 0.575$m for the 200khz spectral component in this example, Moreover, the red line represents the downstream amplitudes computed by combining the initial amplitude from the decomposition and the e^N method. The alignment of these three results suggests that only the initial amplitude is required to predict downstream modal amplitudes and the modal amplitude can be recovered near the branch I location.

Moreover, the modal amplitudes obtained from the decomposition are used to compute the growth rate for the discrete mode S with Eq. (33). Figure 4 compares the DNS growth rate of He and Zhong to the growth rate obtained with the aid of bi-orthogonal decomposition. Near the branch I location, the DNS result of He and Zhong contains high oscillations due to multimode effects. With the bi-orthogonal decomposition, the mode S amplitudes at various locations can be extracted and the oscillation of the resultant growth rate near the branch I location is reduced. Note that near the branch I location, the numerical integration of the decomposition is performed up to the boundary layer edge for the discrete modes. Furthermore, oscillations still exist in the decomposed result primarily due to resolution. More streamwise locations can be sampled to achieve less numerical error in the numerical differentiation for calculating the growth rate. Yet, the current result has demonstrated the capability of recovering the mode S amplitude near the branch I location. Subsequently, the spectral receptivity coefficient for each of the disturbances is calculated from Eq. (42) using decomposed surface pressure perturbation data. Following Eq. (42), the decomposed spectral disturbance data is
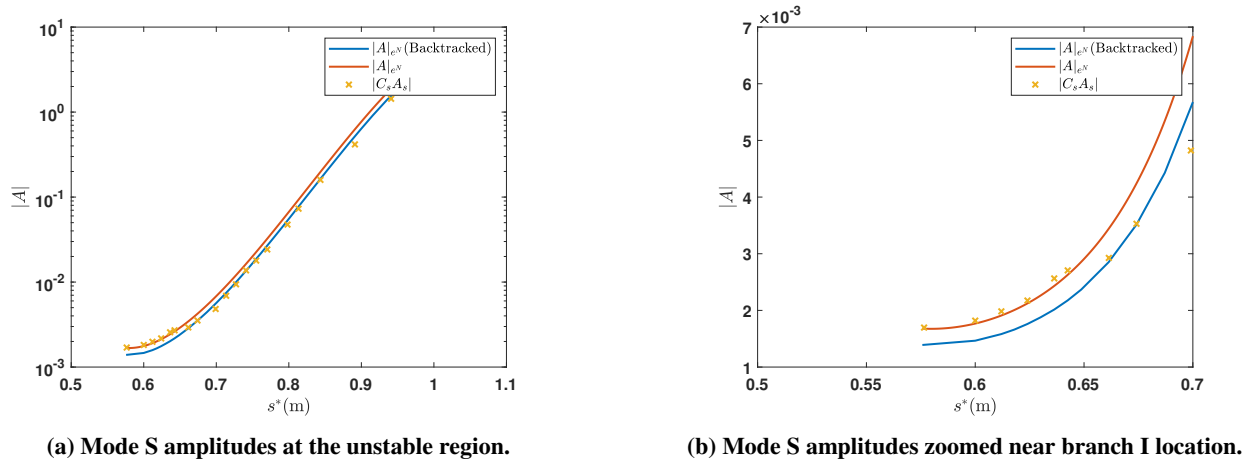
(a) Mode S amplitudes at the unstable region.

(b) Mode S amplitudes zoomed near branch I location.

Fig. 3   Mode S amplitudes at various streamwise locations compared with e^N results

(a) DNS result from He[20].

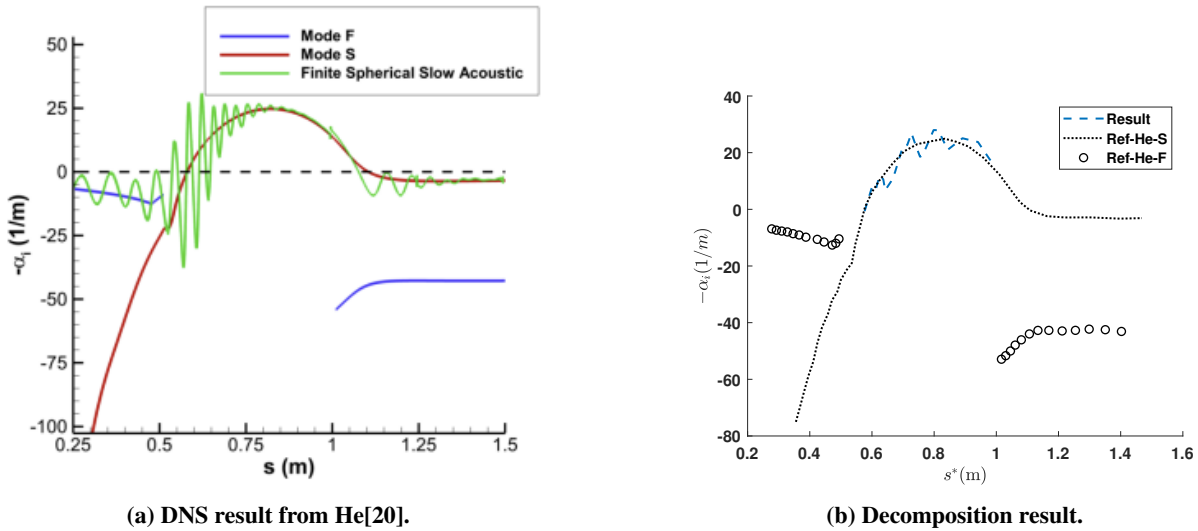**(b) Decomposition result.**

Fig. 4   Mode S growth rate compared with LST results.

normalized by the amplitude spectra of the incident pulse. From He and Zhong [14], the receptivity coefficient obtained with the backtracking method is not a direct evaluation and oscillations in the receptivity coefficient result suggests multimode contribution. Thus, the receptivity coefficient calculated directly using the decomposed mode S amplitude at the branch I neutral stable location is plotted in Fig. 5. From the figure, receptivity coefficients computed using the decomposed amplitude agrees with the overall behavior of the DNS result and demonstrates a smooth trend with frequencies shown. Furthermore, the receptivity coefficient is increasing toward the peak near 240khz, aligning with previous result [20]. Since the paper is a demonstration of the procedure in computing the receptivity coefficient with the aid of bi-orthogonal decomposition, a small band of frequencies with low resolution is applied. The consideration of broader frequency band is necessary to fully recover the true receptivity coefficient for amplitude method.

After computing the growth rate and receptivity coefficients, individual streamwise decompositions are presented with modal eigenfunctions for further investigation. Figure 6 presents the decomposition result at a second-mode dominant location at $s^* = 1.25$m, previously presented in [31]. At this location, the decomposition result indicates that a higher mode S amplitude, aligning with LST. On the other hand, the discrete mode F amplitude is negligible at this region. Similar behavior of small contribution is observed for the continuous fast and slow acoustic modes [31]. The reconstructed signal has a slightly higher amplitude than the FFT result due to numerical errors from the integration [31].
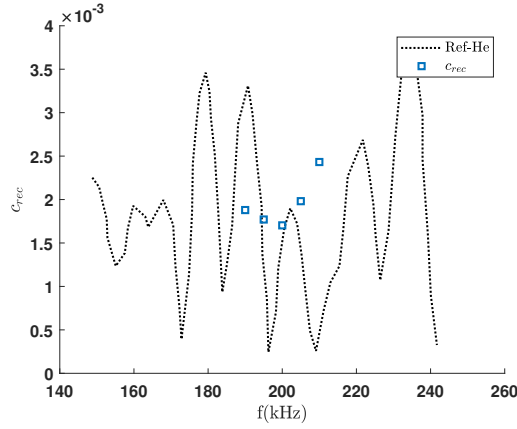
13

Fig. 5   Receptivity coefficients of discrete mode S plotted against results from He [20].

(a) Streamwise Velocity.

(b) Pressure.
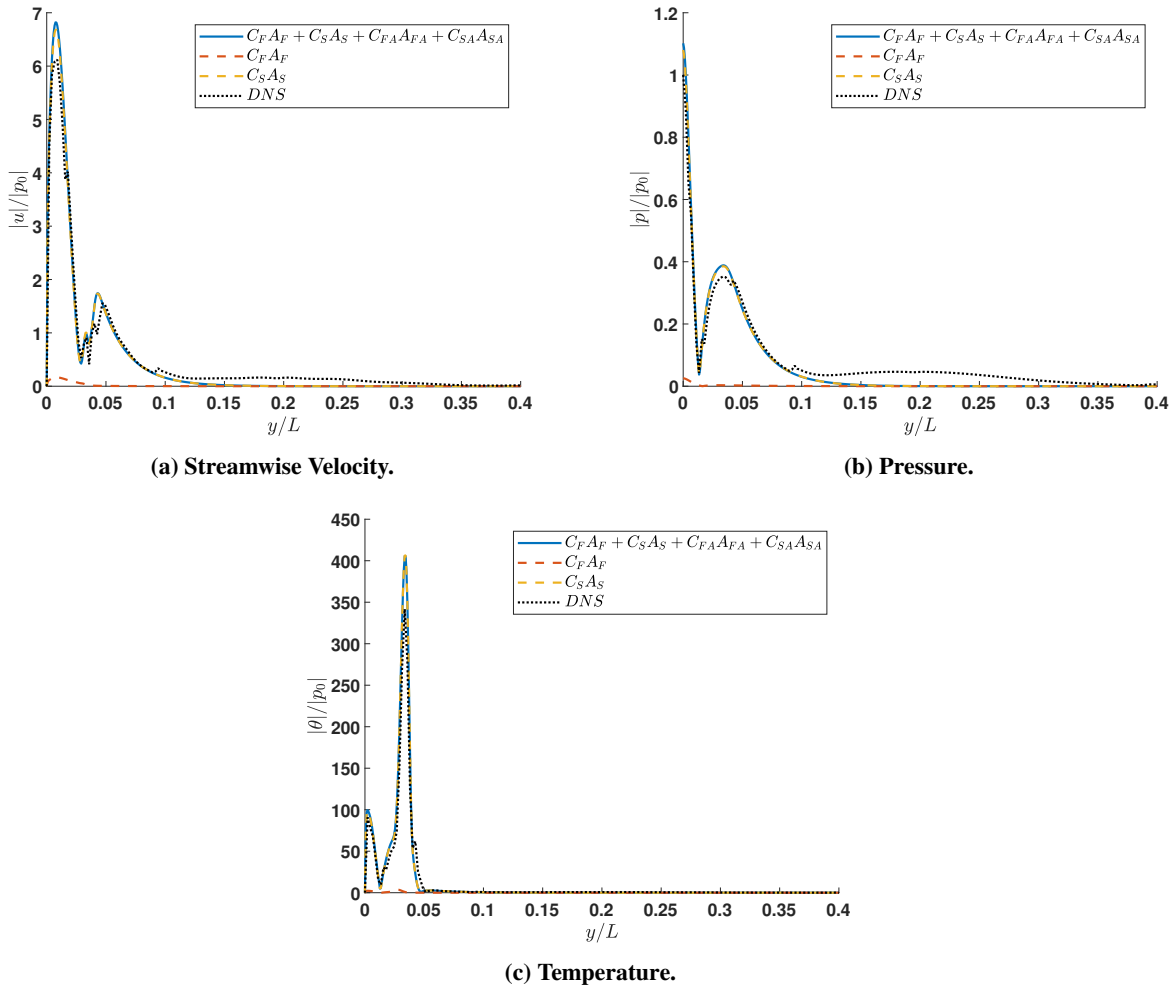

(c) Temperature.

Fig. 6   The streamwise velocity component, pressure, and temperature projection Magnitudes compared with the spectral component of the unsteady DNS data at $s^* = 1.25$m, reproduced from Zou and Zhong [31]

Furthermore, Fig. 7 shows the projection of discrete mode S on to the FFT data at a streamwise location near the branch

I neutral stable location, $s^* = 0.600$m. In contrast with the flowfield at the second-mode dominant region, the flowfeid at the upstream region is more complex, comprising of different peaks inside both the boundary layer and entropy layer around $y/L = 0.2$. From Fig. 6a, the discrete mode S is responsible for the first peak of disturbance inside the boundary layer. However, the discrete mode S decays outside of the boundary layer while the FFT flowfield shows high magnitudes of perturbation. Furthermore, the pressure eigenfunction in Fig. 6b, normalized by the wall pressure, suggests that the wall pressure has a 40 percent contribution from modes other than mode S. The temperature perturbation of Fig. 6c further indicates a high amplitude entropy disturbance exist in this streamwise region. This observation aligns with previous findings in [43] that the mode S instability could be induced by an entropy layer instability mode, referred to as the discrete entropy layer mode in the later section.
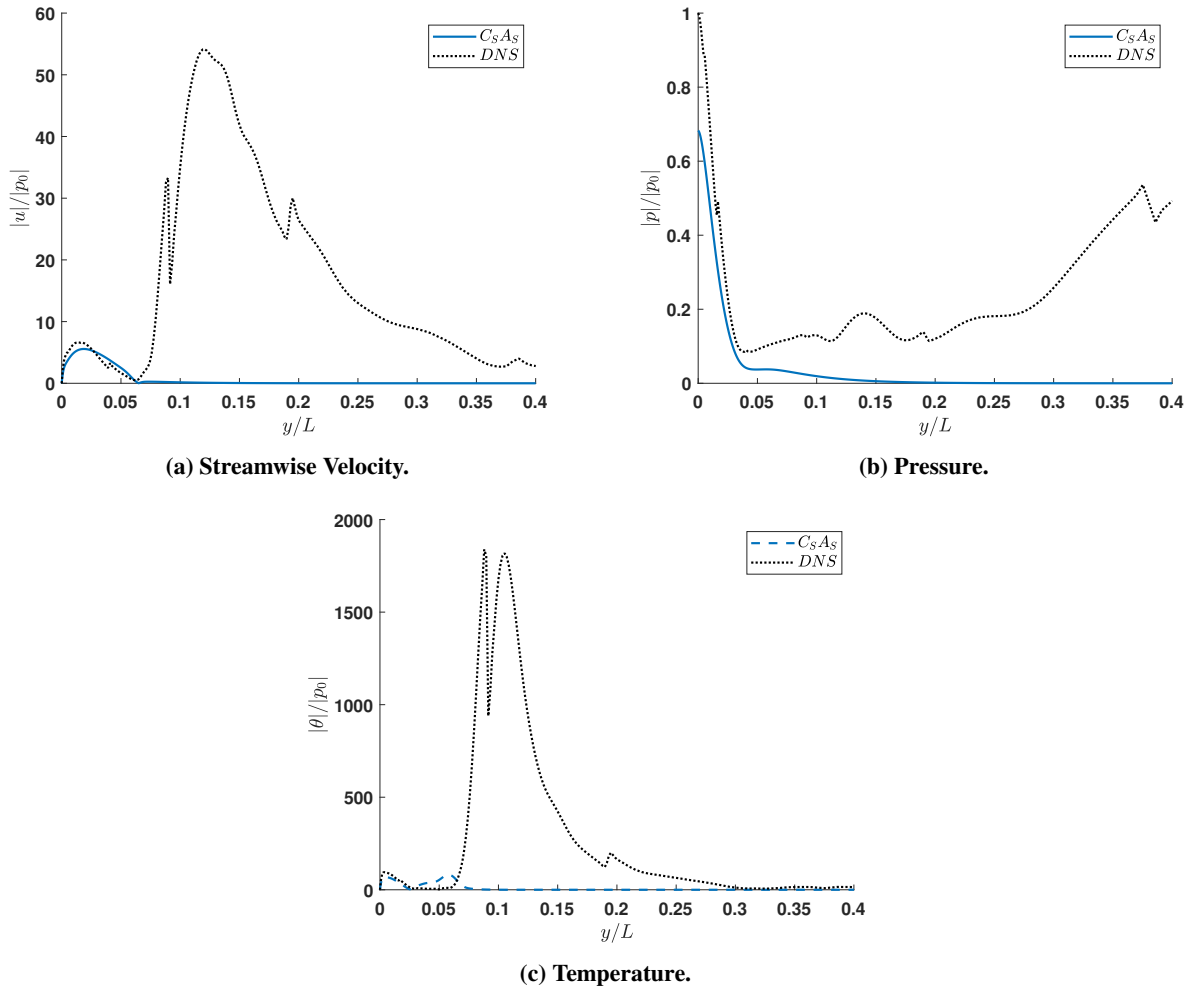

(a) Streamwise Velocity.

(b) Pressure.

(c) Temperature.

Fig. 7 The streamwise velocity component, pressure, and temperature projection Magnitudes compared with the spectral component of the unsteady DNS data at $s^* = 0.600$m.

B. Discrete Entropy Layer Mode

In addition to the analysis of discrete mode S, the flow physics near the synchronization regions of discrete and continuous modes is less understood due to the lack of a multimode decomposition [20]. In these synchronization regions, various discrete and continuous normal modes interact and participate in intermodal energy exchanges. Specifically, the synchronization between the discrete modes F and S is attributed to giving rise to the second mode instability [45] [20]. However, a recent study by Wan, Su, and Chen [43] suggests a possibility of second mode excitation due to the entropy layer instabilities. Thus, the bi-orthogonal decomposition of the unsteady flowfield with three discrete modes: F, S, and

15

a newly discovered entropy-layer mode is performed with the goal to better understand the modal contributions.

In addition to the discrete modes F and S, an entropy layer mode has been identified near the synchronization region. The phase speed and growth rate of the entropy layer mode are plotted over streamwise locations in Fig. 8. From the phase speed plot, a discrete mode that is not modes F and S exists near the synchronization region. This mode emerges upstream and approaches the phase speed of an entropy/vorticity mode ($c_r = 1$). Similarly, the growth rate shows a trend approaching a neutral wave similar to the vorticity and entropy continuous modes. Although such entropy layer mode has been shown to exist before the emergence of discrete mode S in a previous study [44], the current result indicates the possibility of co-existence for a small bluntness.
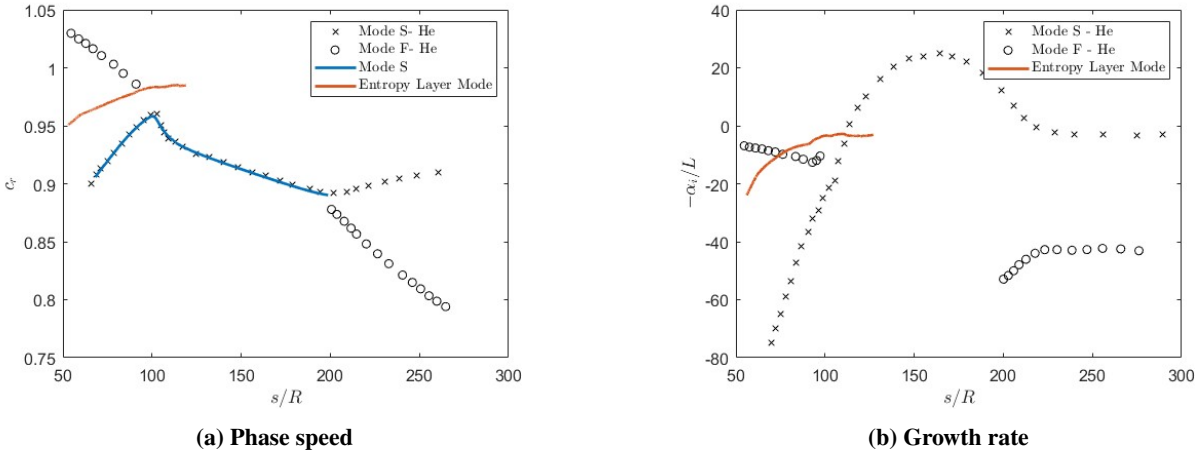

(a) Phase speed

(b) Growth rate

Fig. 8   (a) Phase speed and (b) growth rate of the entropy layer mode plotted against mode S and previous result from He and Zhong [14]

Figure 9 presents the eigenfunctions of the discrete entropy layer mode. From the eigenfunction, the discrete entropy layer mode demonstrates an extended perturbation into the entropy layer around $y/L = 0.15$.
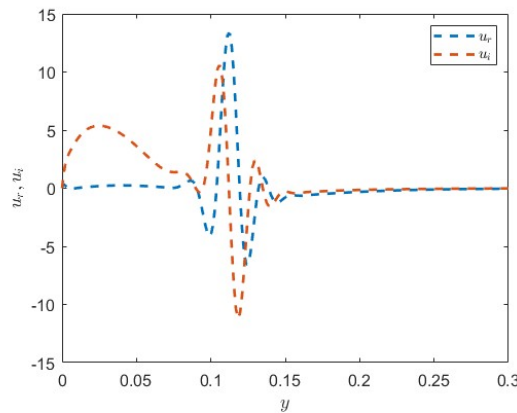

Fig. 9   The streamwise velocity eigenfunction of the new entropy-layer mode at 200 **khz near the synchronization point (**$s^* = 0.4$ **m).**

From the results shown, this discrete mode aligns with the behavior of discrete entropy layer modes described in [44]. The inclusion of this entropy layer mode in the bi-orthogonal decomposition near the synchronization region is also performed. With the discrete modes F, S and the entropy layer mode, Fig. 10 presents the decomposition result of the unsteady flowfield near the synchronization region at 200 khz. A dominance of mode F can be observed inside the boundary layer while the discrete entropy layer mode is responsible for the second peak of the unsteady DNS flowfield. Beyond the second peak of the DNS flow field, wave structures suggest the existence of continuous modes

16

and supersonic modes which require additional investigation [20].

(a) Reconstructed signal
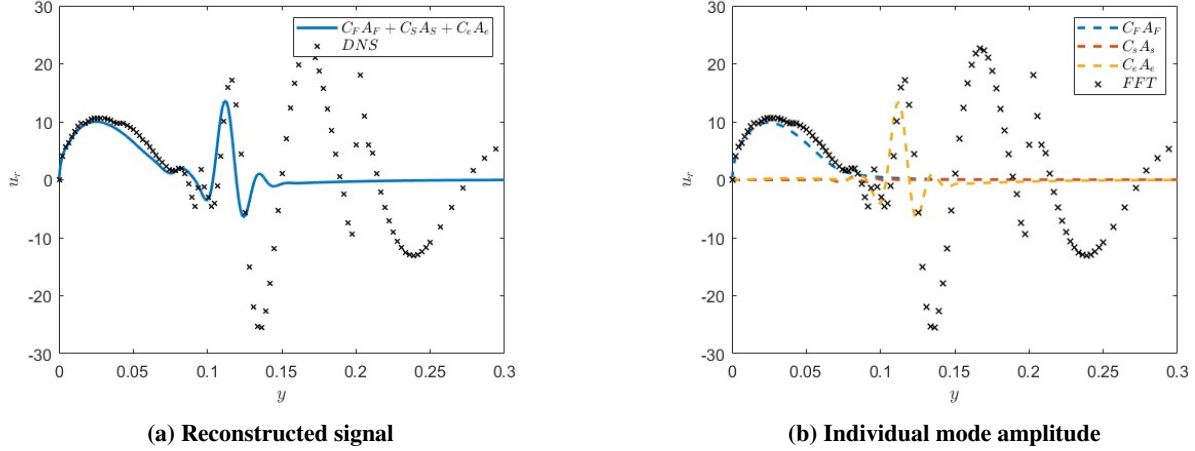

(b) Individual mode amplitude

Fig. 10   Decomposition results with (a) the overall reconstructed signal and (b) individual mode amplitude plotted against the unsteady FFT flowfield at 200 **khz near the synchronization point (**$s^* = 0.4$**m).**

V. Conclusion and Future Work

The bi-orthogonal decomposition of the unsteady DNS flowfield data stemming from a freestream receptivity simulation by He and Zhong [19] has been performed with preliminary results shown. This procedure involved applying the orthogonality relation to Fourier-transformed flowfield data at a specified frequency. By projecting the perturbation variables onto the bi-orthogonal eigenfunctions, the modal perturbation amplitudes can be obtained. Remarkably, from the preliminary results of the mode S decomposition over streamwise locations, an overall trend of the discrete mode S amplitude agrees with previous results. From the growth rate comparison, the bi-orthogonal decomposed result has reduced oscillations near the branch I neutral location than previous DNS results [20] and aligns more with LST. Moreover, the discrete mode S receptivity coefficients for a small band of frequencies are computed and aligns with the trend of previous work while reducing the oscillation. Further consideration of a boarder band of frequencies with higher resolution would be the immediate next step to fully recover the true receptivity coefficient for the amplitude method.

Furthermore, the decomposition results at a downstream location aligned with the observation of the discrete mode S being dominant while the decomposition of the flowfield near the branch I neutral location indicates multimode contribution with perturbations in the entropy layer. In addition, near the synchronization region, the existence of a discrete entropy layer mode is demonstrated. This mode is obtained with the very high-order finite difference scheme proposed by Zou and Zhong [31]. Although such entropy layer mode has been shown to exist before the emergence of discrete mode S in a previous study [44], the current result indicates the possibility of co-existence for a small bluntness. The influence of such disturbance on the transition is limited and needs further investigation. The continuous development of the bi-orthogonal decomposition analysis includes further computation of various higher discrete modes and continuous modes such as entropy and vorticity modes. Moreover, the bi-orthogonal decomposition of various types of freestream broadband disturbances and more streamwise locations would give more insight into the behavior of these discrete and continuous modes. The subsequent implementation of the amplitude method would follow to systematically obtain accurate transition predictions.

A. The Matrix Elements

The matrix elements of $\mathbf{H}_0$ in Eq. (17) are presented here. Similar to Ref. [32], [33], we define $r = 2(\epsilon + 2)/3$ and $m = 2(\epsilon - 1)/3$ where ϵ is the ratio of bulk viscosity to dynamic viscosity and equals to 0 following Stoke's hypothesis. For entries not specified, the coefficients are equal to zero. We first define,

$$\chi = \left[\frac{Re}{\mu} - \frac{i\hat{\omega}r}{P} \right]^{-1}$$

$$\hat{\omega} = \omega - \alpha U.$$

(43)

For $\mathbf{H}_0$, we have

$$H_0^{1,2} = 1$$

$$H_0^{2,1} = \alpha^2 + \beta^2 - i\hat{\omega}P\gamma M^2 \frac{Re}{\mu T}$$

$$H_0^{2,2} = -\frac{1}{\mu} \frac{\partial \mu}{\partial y}$$

$$H_0^{2,3} = -i\alpha(m+1)\frac{1}{T}\frac{\partial T}{\partial y} - i\alpha\frac{1}{\mu}\frac{\partial \mu}{\partial y} + \mathrm{Re}\,P\gamma M^2 \frac{1}{\mu T}\frac{\partial U}{\partial y} + i\alpha(m+1)\frac{1}{P}\frac{\partial P}{\partial y}$$

$$H_0^{2,4} = i\alpha\frac{Re}{\mu} + \alpha\hat{\omega}(m+1)\frac{1}{P}$$

$$H_0^{2,5} = -\alpha\hat{\omega}(m+1)\frac{1}{T} - \frac{1}{\mu}\left(\frac{\partial T}{\partial y}\frac{\partial U}{\partial y}\frac{\partial^2 \mu}{\partial T^2} + \frac{\partial \mu}{\partial T}\frac{\partial^2 U}{\partial y^2}\right)$$

$$H_0^{2,6} = -\frac{1}{\mu}\frac{\partial \mu}{\partial T}\frac{\partial U}{\partial y}$$

$$H_0^{3,1} = -i\alpha$$

$$H_0^{3,3} = \frac{1}{T}\frac{\partial T}{\partial y} - \frac{1}{P}\frac{\partial P}{\partial y}$$

$$H_0^{3,4} = \frac{i\hat{\omega}}{P}$$

$$H_0^{3,5} = -\frac{i\hat{\omega}}{T}$$

$$H_0^{3,7} = -i\beta$$

$$H_0^{4,1} = -i\chi\alpha\left(r\frac{1}{T}\frac{\partial T}{\partial y} + \frac{2}{\mu}\frac{\partial \mu}{\partial y} - r\frac{1}{P}\frac{\partial P}{\partial y}\right)$$

$$H_0^{4,2} = -i\chi\alpha$$

$$H_0^{4,3} = \chi\left(-\alpha^2 - \beta^2 + i\hat{\omega}P\gamma M^2 \frac{Re}{\mu T} + r\frac{1}{T}\frac{\partial^2 T}{\partial y^2} + r\frac{1}{\mu T}\frac{\partial \mu}{\partial y}\frac{\partial T}{\partial y} - r\frac{1}{\mu P}\frac{\partial \mu}{\partial y}\frac{\partial P}{\partial y} + 2r\frac{1}{P^2}\left[\frac{\partial P}{\partial y}\right]^2 - 2r\frac{1}{PT}\frac{\partial P}{\partial y}\frac{\partial T}{\partial y}\right.$$
$$\left. -r\frac{1}{P}\frac{\partial^2 P}{\partial y^2}\right)$$

$$H_0^{4,4} = -i\chi r\frac{1}{P}\left(\alpha\frac{\partial U}{\partial y} - \hat{\omega}\frac{1}{T}\frac{\partial T}{\partial y} - \hat{\omega}\frac{1}{\mu}\frac{\partial \mu}{\partial y} + 2\hat{\omega}\frac{1}{PT}\frac{\partial P}{\partial y}\right)$$

$$H_0^{4,5} = i\chi\left(\alpha r\frac{1}{T}\frac{\partial U}{\partial y} + \alpha\frac{1}{\mu}\frac{\partial \mu}{\partial T}\frac{\partial U}{\partial y} - r\hat{\omega}\frac{1}{\mu T}\frac{\partial \mu}{\partial y} + r\hat{\omega}\frac{1}{PT}\frac{\partial P}{\partial y}\right)$$

$$H_0^{4,6} = -i\chi r\hat{\omega}\frac{1}{T}$$

$$H_0^{4,7} = -i\chi\beta\left(r\frac{1}{T}\frac{\partial T}{\partial y} + 2\frac{1}{\mu}\frac{\partial \mu}{\partial y} - r\frac{1}{P}\frac{\partial P}{\partial y}\right)$$

$$H_0^{4,8} = -i\chi\beta$$

$$H_0^{5,6} = 1$$

$$H_0^{6,2} = -2(\gamma - 1)M^2 \mathrm{Pr}\,\frac{\partial U}{\partial y}$$

18

$$H_0^{6,3} = -2i\alpha(\gamma - 1)M^2 \mathrm{Pr}\, \frac{\partial U}{\partial y} + \mathrm{P}\gamma\, M^2 \mathrm{Pr}\, \frac{\mathrm{Re}}{\mu T}\frac{\partial T}{\partial y} - (\gamma - 1)M^2 \mathrm{Pr}\, \frac{\mathrm{Re}}{\mu}\frac{\partial P}{\partial y}$$

$$H_0^{6,4} = i\hat{\omega}(\gamma - 1)M^2 \mathrm{Pr}\, \frac{\mathrm{Re}}{\mu}$$

$$H_0^{6,5} = \alpha^2 + \beta^2 - i\hat{\omega}\, \mathrm{Pr}\, M^2 \mathrm{Pr}\, \frac{\mathrm{Re}}{\mu T} - (\gamma - 1)M^2 \mathrm{Pr}\, \frac{1}{\mu}\frac{\partial \mu}{\partial T}\left(\frac{\partial U}{\partial y}\right)^2 - \frac{1}{\mu}\frac{\partial^2 \mu}{\partial y^2}$$

$$H_0^{6,6} = -\frac{2}{\mu}\frac{\partial \mu}{\partial y}$$

$$H_0^{7,8} = 1$$

$$H_0^{8,3} = -i\beta(m + 1)\frac{1}{T}\frac{\partial T}{\partial y} - i\beta\frac{1}{\mu}\partial\mu\partial y + i\beta(m + 1)\frac{1}{P}\frac{\partial P}{\partial y}$$

$$H_0^{8,4} = \beta\hat{\omega}(m + 1)\frac{1}{P} + i\beta\frac{Re}{\mu}$$

$$H_0^{8,5} = -\beta\hat{\omega}(m + 1)\frac{1}{T}$$

$$H_0^{8,7} = \alpha^2 + \beta^2 - i\hat{\omega}P\gamma M^2 \frac{Re}{\mu T}$$

$$H_0^{8,8} = -\frac{1}{\mu}\frac{\partial \mu}{\partial y}$$

Acknowledgments

References

[1] V., M., "Transition in open flow systems-a reassessment," *Bull. Am. Phys. Soc.*, Vol. 39, 1994, p. 1882. URL https://cir.nii.ac.jp/crid/1573950400137520256.

[2] Mack, L. M., "Transition and laminar instability," Tech. rep., 1977.

[3] Marineau, E. C., "Prediction Methodology for Second-Mode-Dominated Boundary-Layer Transition in Wind Tunnels," *AIAA Journal*, Vol. 55, No. 2, 2017, pp. 484–499. https://doi.org/10.2514/1.J055061, URL https://doi.org/10.2514/1.J055061.

[4] Reed, H. L., and Saric, W. S., *Receptivity: The Inspiration of Mark Morkovin (Invited)*, 2015. https://doi.org/10.2514/6.2015-2471, URL https://arc.aiaa.org/doi/abs/10.2514/6.2015-2471.

[5] Zhong, X., and Wang, X., "Direct Numerical Simulation on the Receptivity, Instability, and Transition of Hypersonic Boundary Layers," *Annual Review of Fluid Mechanics*, Vol. 44, No. 1, 2012, pp. 527–561. https://doi.org/10.1146/annurev-fluid-120710-101208, URL https://doi.org/10.1146/annurev-fluid-120710-101208.

[6] Goldstein, M., and Hultgren, L. S., "Boundary-layer receptivity to long-wave free-stream disturbances," *Annual Review of Fluid Mechanics*, Vol. 21, No. 1, 1989, pp. 137–166.

[7] Fedorov, A., and Khokhlov, A. P., "Excitation of unstable modes in a supersonic boundary layer by acoustic waves," *Fluid Dynamics*, Vol. 26, 1991, pp. 531–537.

[8] Egorov, I., Fedorov, A., and Nechaev, A., *Receptivity of Supersonic Boundary Layer on a Blunt Plate to Acoustic Disturbances*, ???? https://doi.org/10.2514/6.2004-249, URL https://arc.aiaa.org/doi/abs/10.2514/6.2004-249.

[9] Qin, F., and Wu, X., "Response and receptivity of the hypersonic boundary layer past a wedge to free-stream acoustic, vortical and entropy disturbances," *Journal of Fluid Mechanics*, Vol. 797, 2016, p. 874–915. https://doi.org/10.1017/jfm.2016.287.

[10] Marineau, E. C., Moraru, G. C., Lewis, D. R., Norris, J. D., Lafferty, J. F., Wagnild, R. M., and Smith, J. A., *Mach 10 Boundary Layer Transition Experiments on Sharp and Blunted Cones (Invited)*, 2014. https://doi.org/10.2514/6.2014-3108, URL https://arc.aiaa.org/doi/abs/10.2514/6.2014-3108.

[11] Marineau, E. C., Moraru, G. C., Lewis, D. R., Norris, J. D., Lafferty, J. F., and Johnson, H. B., *Investigation of Mach 10 Boundary Layer Stability of Sharp Cones at Angle-of-Attack, Part 1: Experiments*, 2015. https://doi.org/10.2514/6.2015-1737, URL https://arc.aiaa.org/doi/abs/10.2514/6.2015-1737.

[12] Zhong, X., "High-Order Finite-Difference Schemes for Numerical Simulation of Hypersonic Boundary-Layer Transition," *Journal of Computational Physics*, Vol. 144, No. 2, 1998, pp. 662–709. https://doi.org/https://doi.org/10.1006/jcph.1998.6010, URL https://www.sciencedirect.com/science/article/pii/S0021999198960107.

[13] Ma, Y., and Zhong, X., "Receptivity of a supersonic boundary layer over a flat plate. Part 1. Wave structures and interactions," *Journal of Fluid Mechanics*, Vol. 488, 2003, p. 31–78. https://doi.org/10.1017/S0022112003004786.

[14] He, S., and Zhong, X., "Hypersonic Boundary-Layer Receptivity over a Blunt Cone to Freestream Pulse Disturbances," *AIAA Journal*, Vol. 59, No. 9, 2021, pp. 3546–3565. https://doi.org/10.2514/1.J059697, URL https://doi.org/10.2514/1.J059697.

[15] Zhong, X., "Leading-edge receptivity to free-stream disturbance waves for hypersonic flow over a parabola," *Journal of Fluid Mechanics*, Vol. 441, 2001, p. 315–367. https://doi.org/10.1017/S0022112001004918.

[16] Fedorov, A., and Tumin, A., "High-Speed Boundary-Layer Instability: Old Terminology and a New Framework," *AIAA Journal*, Vol. 49, No. 8, 2011, pp. 1647–1657. https://doi.org/10.2514/1.J050835, URL https://doi.org/10.2514/1.J050835.

[17] Huang, Y., and Zhong, X., "Numerical Study of Hypersonic Boundary-Layer Receptivity with Freestream Hotspot Perturbations," *AIAA Journal*, Vol. 52, No. 12, 2014, pp. 2652–2672. https://doi.org/10.2514/1.J052657, URL https://doi.org/10.2514/1.J052657.

[18] He, S., and Zhong, X., *Numerical Study of the Receptivity of a Blunt Cone to Freestream Pulse Disturbances in Hypersonic Flow*, AIAA, 2021. https://doi.org/10.2514/6.2021-2887, URL https://arc.aiaa.org/doi/abs/10.2514/6.2021-2887.

[19] He, S., and Zhong, X., "The effects of nose bluntness on broadband disturbance receptivity in hypersonic flow," *Physics of Fluids*, Vol. 34, No. 5, 2022, p. 054104. https://doi.org/10.1063/5.0088236, URL https://doi.org/10.1063/5.0088236.

[20] He, S., "Receptivity of Straight Blunt Cones to Broadband Freestream Pulse Disturbances for Transition Prediction in Hypersonic Flow," Ph.D. thesis, 2022. URL https://www.proquest.com/dissertations-theses/receptivity-straight-blunt-cones-broadband/docview/2741040054/se-2, copyright - Database copyright ProQuest LLC; ProQuest does not claim copyright in the individual underlying works; Last updated - 2023-03-08.

[21] Salwen, C. E., H.and Grosch, "The continuous spectrum of the Orr-Sommerfeld equation. Part 2. Eigenfunction expansions," *Journal of Fluid Mechanics*, Vol. 104, 1981, p. 445–465. https://doi.org/10.1017/S0022112081002991.

[22] Tumin, A., and Fedorov, A., "Spatial growth of disturbances in a compressible boundary layer," *Journal of Applied Mechanics and Technical Physics*, Vol. 24, No. 4, 1983, pp. 548–554. https://doi.org/10.1007/BF00907906.

[23] Mack, L. M., "Boundary-layer linear stability theory," Tech. rep., California Inst of Tech Pasadena Jet Propulsion Lab, 1984.

[24] Fedorov, A., and Khokhlov, A., "Prehistory of Instability in a Hypersonic Boundary Layer," *Theoretical and Computational Fluid Dynamics*, Vol. 14, 2001, pp. 359–375. https://doi.org/10.1007/s001620100038.

[25] Tumin, A., "The biorthogonal eigenfunction system of linear stability equations: A survey of applications to receptivity problems and to analysis of experimental and computational results." *41st AIAA Fluid Dynamics Conference and Exhibit*, 2011, p. 3244.

[26] Saikia, B., Al Hasnine, S., and Brehm, C., "On the role of discrete and continuous modes in a cooled high-speed boundary layer flow," *Journal of Fluid Mechanics*, Vol. 942, 2022, p. R7. https://doi.org/10.1017/jfm.2022.380.

[27] Hasnine, S. M. A. A., Russo, V., Browne, O. M., Tumin, A., and Brehm, C., *Disturbance Flow Field Analysis of Particulate Interaction with High Speed Boundary Layers*, AIAA, 2020. https://doi.org/10.2514/6.2020-3046, URL https://arc.aiaa.org/doi/abs/10.2514/6.2020-3046.

[28] Ulker, E., Klentzman, J., and Tumin, A., *Stability of Boundary Layers in Binary Mixtures of Oxygen and Nitrogen*, 2011. https://doi.org/10.2514/6.2011-370, URL https://arc.aiaa.org/doi/abs/10.2514/6.2011-370.

[29] Klentzman, J., Ulker, E., and Tumin, A., *Projection of the Solution of the Linearized Navier-Stokes Equations in Reacting High Speed Boundary Layers onto Discrete Modes*, 2012. https://doi.org/10.2514/6.2012-3149, URL https://arc.aiaa.org/doi/abs/10.2514/6.2012-3149.

[30] Luna, K., and Tumin, A., *Three-Dimensional Spatial Normal Modes and Multimode Decomposition for Reacting Boundary Layers*, 2023. https://doi.org/10.2514/6.2023-1625, URL https://arc.aiaa.org/doi/abs/10.2514/6.2023-1625.

[31] Zou, Z., and Zhong, X., *A High-Order Finite-Difference Method for Linear Stability Analysis and Bi-orthogonal Decomposition of Hypersonic Boundary Layer Flow*, 2023. https://doi.org/10.2514/6.2023-1043, URL https://arc.aiaa.org/doi/abs/10.2514/6.2023-1043.

[32] Miselis, M., Huang, Y., and Zhong, X., *Modal Analysis of Receptivity Mechanisms for a Freestream Hot-Spot Perturbation on a Blunt Compression-Cone Boundary Layer*, AIAA, 2016. https://doi.org/10.2514/6.2016-3345, URL https://arc.aiaa.org/doi/abs/10.2514/6.2016-3345.

[33] Tumin, A., "Three-dimensional spatial normal modes in compressible boundary layers," *Journal of Fluid Mechanics*, Vol. 586, 2007, pp. 295–322.

[34] Kosloff, D., and Tal-Ezer, H., "A Modified Chebyshev Pseudospectral Method with an O(N-1) Time Step Restriction," *Journal of Computational Physics*, Vol. 104, No. 2, 1993, pp. 457–469. https://doi.org/https://doi.org/10.1006/jcph.1993.1044, URL https://www.sciencedirect.com/science/article/pii/S0021999183710442.

[35] Zhong, X., and Tatineni, M., "High-order non-uniform grid schemes for numerical simulation of hypersonic boundary-layer stability and transition," *Journal of Computational Physics*, Vol. 190, No. 2, 2003, pp. 419–458. https://doi.org/https://doi.org/10.1016/S0021-9991(03)00282-1, URL https://www.sciencedirect.com/science/article/pii/S0021999103002821.

[36] Shukla, R. K., Tatineni, M., and Zhong, X., "Very high-order compact finite difference schemes on non-uniform grids for incompressible Navier–Stokes equations," *Journal of Computational Physics*, Vol. 224, No. 2, 2007, pp. 1064–1094. https://doi.org/https://doi.org/10.1016/j.jcp.2006.11.007, URL https://www.sciencedirect.com/science/article/pii/S0021999106005663.

[37] Malik, M., "Numerical methods for hypersonic boundary layer stability," *Journal of Computational Physics*, Vol. 86, No. 2, 1990, pp. 376–413. https://doi.org/https://doi.org/10.1016/0021-9991(90)90106-B, URL https://www.sciencedirect.com/science/article/pii/002199919090106B.

[38] Tumin, A., Amitay, M., Cohen, J., and De Zhou, M., "A normal multimode decomposition method for stability experiments," *Physics of Fluids*, Vol. 8, No. 10, 1996, pp. 2777–2779. https://doi.org/10.1063/1.869062, URL https://doi.org/10.1063/1.869062.

[39] Balakumar, P., and Chou, A., "Transition Prediction in Hypersonic Boundary Layers Using Receptivity and Freestream Spectra," *AIAA Journal*, Vol. 56, No. 1, 2018, pp. 193–208. https://doi.org/10.2514/1.J056040, URL https://doi.org/10.2514/1.J056040.

[40] Lei, J., and Zhong, X., "Linear Stability Analysis of Nose Bluntness Effects on Hypersonic Boundary Layer Transition," *Journal of Spacecraft and Rockets*, Vol. 49, 2012, pp. 24–37. https://doi.org/10.2514/1.52616.

[41] Stetson, K., *Laminar boundary layer stability experiments on a cone at Mach 8. II- Blunt cone*, ???? https://doi.org/10.2514/6.1984-6, URL https://arc.aiaa.org/doi/abs/10.2514/6.1984-6.

[42] Dietz, G., and Hein, S., "Entropy-layer instabilities over a blunted flat plate in supersonic flow," *Physics of Fluids*, Vol. 11, No. 1, 1999, pp. 7–9. https://doi.org/10.1063/1.869899, URL https://doi.org/10.1063/1.869899.

[43] Wan, B., Su, C., and Chen, J., "Receptivity of a Hypersonic Blunt Cone: Role of Disturbances in Entropy Layer," *AIAA Journal*, Vol. 58, No. 9, 2020, pp. 4047–4054. https://doi.org/10.2514/1.J058816, URL https://doi.org/10.2514/1.J058816.

[44] Wan, B., Chen, J., Tu, G., Xiang, X., Yuan, X., and Duan, M., "Effects of nose bluntness on entropy-layer stabilities over cones and wedges," *Acta Mechanica Sinica*, Vol. 39, No. 1, 2023, 122176. https://doi.org/10.1007/s10409-022-22176-x.

[45] Fedorov, A., "Receptivity of a high-speed boundary layer to acoustic disturbances," *Journal of Fluid Mechanics*, Vol. 491, 2003, p. 101–129. https://doi.org/10.1017/S0022112003005263.